ADVANCING EARTH AND SPACE SCIENCES

JGR Space Physics

RESEARCH ARTICLE
10.1029/2025JA033898

Electron Acceleration and Zebra Stripe Formation in Saturn's Radiation Belts

A. Y. Drozdov[1], P. Kollmann[2], Y. Hao[3,4], D. Wang[4], and E. E. Woodfield[5]

[1]University of California, Los Angeles, CA, USA, [2]Johns Hopkins University Applied Physics Laboratory, Laurel, MD, USA, [3]Max Planck Institute for Solar System Research, Göttingen, Germany, [4]GFZ Helmholtz Centre for Geosciences, Potsdam, Germany, [5]British Antarctic Survey, Cambridge, UK

Key Points:

- The zebra stripe signature in Saturn's radiation belts is reproduced using the Versatile Electron Radiation Belt convection-diffusion code
- Local diffusion, particularly due to chorus and hiss waves, counteract zebra stripe formation and further enhance electron acceleration
- Interplay between dynamic electric field and local wave-particle interactions is crucial for understanding Saturn's radiation belt dynamics

Supporting Information:

Supporting Information may be found in the online version of this article.

Correspondence to:

A. Y. Drozdov,
adrozdov@ucla.edu

Citation:

Drozdov, A. Y., Kollmann, P., Hao, Y., Wang, D., & Woodfield, E. E. (2025). Electron acceleration and zebra stripe formation in Saturn's radiation belts. *Journal of Geophysical Research: Space Physics*, *130*, e2025JA033898. https://doi.org/10.1029/2025JA033898

Received 27 FEB 2025
Accepted 12 APR 2025

Author Contributions:

Conceptualization: A. Y. Drozdov, P. Kollmann
Funding acquisition: A. Y. Drozdov, P. Kollmann
Investigation: A. Y. Drozdov
Methodology: A. Y. Drozdov, P. Kollmann, Y. Hao, E. E. Woodfield
Project administration: P. Kollmann
Resources: Y. Hao, D. Wang, E. E. Woodfield
Software: A. Y. Drozdov
Visualization: A. Y. Drozdov
Writing – original draft: A. Y. Drozdov, P. Kollmann, E. E. Woodfield
Writing – review & editing: A. Y. Drozdov, P. Kollmann, D. Wang

Abstract This study uses the Versatile Electron Radiation Belt code to model Saturn's radiation belt environment, investigating electron acceleration, loss, and transport mechanisms. The simulations consider various physical processes, including convection particularly driven by a Volland-Stern (VS) electric field, radial diffusion, collisional energy loss, and local wave-particle diffusion driven by chorus and hiss waves. Starting from initial conditions derived from Cassini observations, our simulations successfully reproduce the characteristic “zebra stripes” pattern in spectrograms of Saturn's radiation belts. Our results suggest that radial diffusion and neutral-particle interactions have negligible effects on zebra stripe formation. However, the presence of a persistent VS electric field results in significant electron acceleration above the Corotation Drift Resonance energies in the MeV energy range, producing flux levels exceeding typical observations. Additional local wave-particle diffusion further enhances electron acceleration in this energy range. When the VS electric field pulse is treated as transient instead of constant to imitate dynamic conditions, the overestimation of MeV electron flux is reduced near $L \sim 5$ but remains elevated and further enhanced near $L \sim 8$. Despite these differences, the simulations underscore the critical role of the VS electric field and local diffusion in controlling electron acceleration and transport. Our results highlight the necessity of understanding the interplay between global electric fields and localized diffusion processes in shaping electron dynamics within Saturn's radiation belts.

Plain Language Summary Saturn's radiation belts contain high-energy electrons that can be transported and accelerated through interactions with the planet's electric and magnetic fields, as well as with plasma waves. This study uses modeling to explore how these electrons behave, with a focus on a pattern called “zebra stripes.” The results indicate that a large-scale electric field plays a dominant role in shaping the electron energy spectrum, while interactions with plasma waves further accelerate electrons and redistribute their energy. These findings enhance our understanding of Saturn's radiation belts dynamics.

1. Introduction

Saturn's radiation belts present an unique environment for studying electron acceleration and the overall behavior of planetary radiation belts. Observations from the Cassini mission have revealed complex electron belt features, including the notable “zebra stripes” signature, previously observed at Earth (e.g., Liu et al., 2016; Ukhorskiy et al., 2014). Zebra stripes refer to distinct electron flux enhancements across different energy levels with a pattern resembling the stripes of a zebra when displayed in energy versus time spectrograms where intensity is shown as color-coding (see Figure 2c, for example). This signature is associated to variations in azimuthal electric fields and particle drift (Sun et al., 2019). This phenomenon has been successfully reproduced in test-particle simulations (Hao et al., 2020).

However, the radiation belt environment at Saturn results from the interplay of multiple competing physical processes, balancing electron acceleration and loss mechanisms. Various loss mechanisms, such as ionization energy loss from neutral-charged and charged-charged particle collisions, and pitch-angle diffusion due to the same collisons as well as wave-particle interactions, limit or even counteract acceleration mechanisms like radial diffusion, adiabatic acceleration, and energy diffusion driven by wave-particle interactions (e.g., Horne et al., 2008; Kollmann et al., 2011, 2013; Roussos et al., 2014; Shprits et al., 2012; Woodfield et al., 2019). While adiabatic acceleration associated with radial diffusion has been extensively studied (see Lejosne & Kollmann, 2020), it remains an active area of research, particularly regarding its role in shaping the dynamics of

Saturn's radiation belts. In contrast, the role of large-scale electric fields in driving convective transport is less well understood (e.g., Hao et al., 2020; Roussos et al., 2018; Sun et al., 2019). This transport mechanism significantly influences the dynamics of Saturn's radiation belts, but its impact on electron populations is not fully characterized.

For example, under stationary electric and magnetic conditions, a distinct population of electrons exists, where the gradient-curvature drift is balanced by the azimuthal drift induced by the electric field. These electrons are in Corotation Drift Resonance (CDR), with their energies aligning closely with the observed spectral cutoff of electrons. Electrons near CDR are sensitive to being radially transported through by additional non-radial electric field components (Roussos et al., 2018). Test-particle simulations indicate that such electric fields can effectively drive adiabatic acceleration (e.g., Hao et al., 2020), providing insights into particle energization mechanisms, but cannot explain the near-absence of electrons beyond CDR energy (Sun et al., 2019). One possible explanation may be that conventional test-particle simulations do not account for local diffusion effects caused by wave-particle interactions. Conversely, simulations based on the Fokker-Planck equation, which include local diffusion, demonstrate that electron acceleration is efficiently driven by chorus waves (e.g., Shprits et al., 2012; Woodfield et al., 2019). A comprehensive model that incorporates both large-scale and localized interactions is necessary to enhance our understanding of Saturn's radiation belt dynamics.

The Versatile Electron Radiation Belt (VERB) code, which solves the three-dimensional Fokker-Planck equation, has been widely used to model Earth's radiation belts (e.g., Drozdov et al., 2017, 2020, 2021; Saikin et al., 2021; Shprits et al., 2008, 2009; Subbotin & Shprits, 2009, 2012). This model was later extended to the VERB-4D code, which accounts for the drift phase of electrons by including additional advection terms, such as radial and azimuthal convection (Aseev et al., 2016; Shprits et al., 2015).

In this study, we adapted the VERB-4D code to comprehensively model Saturn's radiation belts. Our analysis examines the contributions of radial diffusion, collisional energy loss, alongside the effects of the Volland-Stern (VS) electric field and wave-particle interactions, particularly those caused by chorus and hiss waves, on the distribution and acceleration of electrons in Saturn's radiation belts.

2. Data and Methodology

To perform the modeling, we rely on measurements obtained by the Cassini satellite. We use these data to establish initial and boundary conditions for our simulations, compare expected simulation results with observational patterns. This section describes the measurements, the modeling framework, and the key assumptions used in our simulations.

2.1. Cassini Data

In this study, we use data from the Cassini mission, focusing on measurements from the Low Energy Magnetospheric Measurement System (LEMMS), part of the Magnetospheric Imaging Instrument (MIMI) package (Krimigis et al., 2004). LEMMS detects electrons across an energy spectrum ranging from tens of keV to several MeV (30 keV–20 MeV) (Krupp, Roussos, et al., 2018). The electron flux is derived from high-resolution electron channels (PHE-E and PHA-F1), that reach up to 1.6 MeV and overlap within the 140–420 keV range. However, there are discrepancies in their flux values within the overlapped region due to contamination from penetrating MeV electrons and low counting statistics. To mitigate these discrepancies, we normalize the PHE-F1 channel flux at 200 keV (with corresponding ratio of 0.83 ± 0.41, depending on L) to align with the corresponding PHE-E channel value. This normalization ratio is then applied to adjust the spectrum above 200 keV accordingly. The processed data set is subsequently used to establish initial and boundary conditions for our simulations.

2.2. The Versatile Electron Radiation Belt Code

For this study, we adapted the four-dimensional (4D) version of the VERB code (Aseev et al., 2016; Shprits et al., 2015; Subbotin & Shprits, 2009) to model the transport, acceleration, and loss processes driving Saturn's radiation belts dynamics. Unlike earlier approaches based on tracing single particles (Hao et al., 2020; Roussos et al., 2018), our method solves a form of the Fokker-Planck equation to simulate the evolution of the full phase space density f. This allows us to include physical processes beyond convective transport, including contributions of diffusion processes. The simplified equation that accounts for convection, radial diffusion, and potential loss mechanisms is expressed as:

$$\frac{\partial f}{\partial t} = -\langle v_\Phi \rangle \frac{\partial f}{\partial \Phi} - \langle v_R \rangle \frac{\partial f}{\partial R} + \frac{1}{G}\frac{\partial}{\partial L} G \langle D_{LL} \rangle \frac{\partial f}{\partial L} - \frac{f}{\tau} \tag{1}$$

where Φ represents the azimuthal coordinate, R is the radial distance from Saturn, L denotes the dipole L-shell (equal to R in the equatorial plane in the dipole field), and G is the Jacobian of the selected coordinate system. The terms $\langle v_\Phi \rangle$ and $\langle v_R \rangle$ are the azimuthal and radial bounce-averaged drift velocities, respectively; $\langle D_{LL} \rangle$ is the radial diffusion coefficient, and τ represents the loss term.

We use Equation 1 to investigate the formation of zebra stripe patterns in Saturn's radiation belts, focusing on the roles of radial diffusion and electron interactions with neutrals. This approach provides an approximation of the potential impact of additional processes on the zebra stripe pattern formation and evolution. Furthermore, simulations based on Equation 1 are conducted to validate that our model can reproduce the zebra stripe structures previously replicated using test-particle simulations.

To account for local diffusion, we introduce terms representing energy and pitch-angle scattering in modified adiabatic invariants V–K space (Subbotin & Shprits, 2012), where $K = \int s\sqrt{B_m - B(s)}ds$; $V = \mu \cdot (K + 0.5)^2$, μ is the first adiabatic invariant, B is magnetic field along the field line s with value at the mirror points B_m. This approach is chosen as it eliminates the need for interpolation between radial and local grids in comparison to the traditional approach, when the local diffusion is solved in energy and pitch angle space. The additional diffusion terms are expressed as:

$$\begin{aligned} \frac{\partial f}{\partial t} = \ldots\ & + \frac{1}{G}\frac{\partial}{\partial V}\left[G\left(\langle D_{VV}\rangle \frac{\partial f}{\partial V} + \langle D_{VK}\rangle \frac{\partial f}{\partial K}\right)\right] \\ & + \frac{1}{G}\frac{\partial}{\partial K}\left[G\left(\langle D_{KK}\rangle \frac{\partial f}{\partial K} + \langle D_{VK}\rangle \frac{\partial f}{\partial V}\right)\right] \\ & - \frac{f}{\tau_{lc}} \end{aligned} \tag{2}$$

where $\langle D_{VV}\rangle$, $\langle D_{KK}\rangle$, and $\langle D_{VK}\rangle$ are coefficients that describe bounce-averaged diffusion of the adiabatic invariants in a way that is equivalent to energy, pitch-angle, and mixed local diffusion. The term τ_{lc} denotes the loss timescale due to atmospheric interactions and is set to one-quarter of the electron bounce period and replaces τ in Equation 1. In this model, we assume that particles are lost when they reach an altitude equal to Saturn's average radius (60,268 km). By incorporating both convection and local diffusion processes, the model provides a more comprehensive representation of particle transport. Extending Equation 1 to incorporate additional terms, we account for both convection and local diffusion processes. Thus, the VERB-4D code allows us to explore interactions with plasma waves such as chorus and hiss, along with other dynamic processes affecting electron behavior. These improvements are important for better understanding of electron dynamics in Saturn's radiation belts.

Our simulations focus on the L-shell range from 4 to 10, with typical boundary conditions (Subbotin & Shprits, 2009; Woodfield et al., 2019). The inner boundary is placed at $L = 4$ because the measurements to be compared to become increasingly unreliable further in. Phase space densities are relatively low in this region (Kollmann et al., 2013), which we approximate here as 0. The outer boundary at $L = 10$ reflects constraints imposed by Saturn's non-dipolar magnetic field (Carbary et al., 2009) and the limited detailed electric field measurements beyond this region. The outer boundary conditions are held constant, corresponding to the average phase space density in the initial conditions. The initial conditions are based on mission-averaged observations (Section 2.1) and illustrated in the left column of Figures 2 and 4.

2.3. Convection and Radial Diffusion

We assume a dipole magnetic field, which is appropriate for the L-shell range between 4 and 10 and is suitable for investigating the formation of the zebra stripe signature and understanding electron acceleration mechanisms. To account for electric fields, we use the VS and rigid corotation models, following Hao et al. (2020). The non-radial VS electric field is assumed to be directed noon-to-midnight and parameterized as:

$$\begin{aligned} E_R^{VS} &= -1 \cdot E_0 (R/L_0)^{\gamma-1} \cdot (\gamma \sin(\Phi + \pi/2)) \\ E_\Phi^{VS} &= -1 \cdot E_0 (R/L_0)^{\gamma-1} \cdot (\cos(\Phi + \pi/2)) \\ E_0 &= 0.3 \text{ mV/m}, \quad \gamma = 0.5 \end{aligned} \tag{3}$$

where E_R^{VS} and E_Φ^{VS} represent the radial and azimuthal components of the VS electric field, as illustrated in Figure S1 in Supporting Information S1. Here, E_0 denotes the noon-to-midnight electric field amplitude, while γ is an index controlling the spatial variation of the electric field, describing its observed decrease with L (Hao et al., 2020). The electric field amplitude and L-shell dependence are selected to be consistent with previous test-particle simulations, which are generally consistent with observations (e.g., Andriopoulou et al., 2014). The chosen amplitude is higher than the average. However, it is worth noting that the electric field strength can vary significantly, with some cases exceeding 0.6 mV/m.

The radial corotation electric field (also shown in Figure S1 in Supporting Information S1), E_R^C, has only a radial component and is defined following Andriopoulou et al. (2012) and Paranicas et al. (2010):

$$\begin{aligned} E_R^C &= \Omega \cdot B_0 \cdot R_s / R^2 \\ B_0 &= 0.215 \times 10^{-4} \text{ T} \\ \Omega &= 1.62 \times 10^{-4} \text{ s}^{-1} \end{aligned} \tag{4}$$

where B_0 represents Saturn's equatorial surface magnetic field and Ω is the corotation frequency.

For simplicity and because we are not aiming to reproduce measurements from a specific Cassini orbit, we ignore here the small-scale electric fields that are set up from injections resulting from centrifugally driven interchange (e.g., Paranicas et al., 2020).

The total radial E_R and azimuthal E_Φ electric fields used in the simulations are defined as:

$$\begin{aligned} E_\Phi &= E_\Phi^{VS} \\ E_R &= E_R^{VS} + E_R^C \end{aligned} \tag{5}$$

Equation 1 does not explicitly include electric and magnetic fields but instead operates with the radial $\langle v_R \rangle$ and azimuthal $\langle v_\Phi \rangle$ velocities. While the radial velocity is primarily driven by the $\mathbf{E} \times \mathbf{B}$ drift, the azimuthal velocity also accounts for the effects of magnetic gradient-curvature drift. These calculated velocities, along with their individual components, are discussed in Text S1 in Supporting Information S1 and illustrated in Figure S2 in Supporting Information S1.

The radial diffusion coefficient is parameterized as in Kollmann et al. (2011). Diffusion coefficients were determined from instances where Cassini crossed the orbits of several moons and observed signatures of the respective moons absorbing electrons. These absorption signatures refilled via radial diffusion, which allowed to estimate the diffusion coefficient Roussos et al. (2007). The single diffusion coefficients were then fit with a L-dependent function. Figure 1a illustrates the radial diffusion coefficient as a function of L:

$$D_{LL} = 2 \cdot 10^{-14} \cdot L^7 \text{ s}^{-1} \tag{6}$$

Even though the absorption of electrons at moons can be used to quantify radial diffusion, this absorption does not yield significant absorption signatures at all local times (which would in the measurements, such as the left column in Figure 2). We therefore neglect the absorption of electrons at the moons.

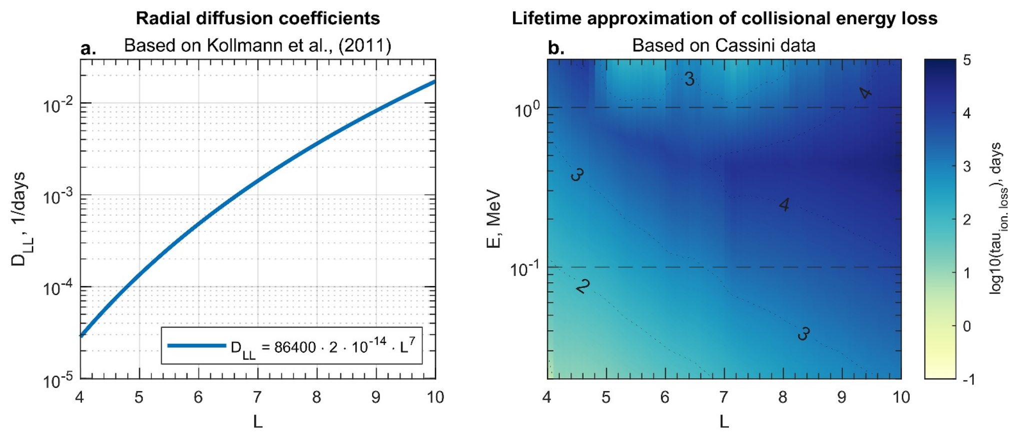

Figure 1. (a) The radial diffusion coefficient, derived from Cassini particle measurements (Kollmann et al., 2011); (b) Approximation of the lifetime due to collisional energy loss based on Cassini observations.

2.4. Collisional Energy Loss Approximation

Saturn's moon Enceladus is located near $L = 4$. The direct loss of electrons to the moon is only evident in its immediate environment (e.g., Jones et al., 2006) and not included in our simulation. However, Enceladus releases gas and dust, some of which falls back due to gravity, while the rest forms the Neutral Torus (Smith et al., 2010) and E-ring (Kempf et al., 2010). Energetic particles interact with this material, gradually losing energy when colliding with its particles and ionizing them in the process. In this study, we neglect any changes in pitch angle resulting from these collisions. We also focus on interaction with gas, which has been shown to dominate over the dust at $L = 7$ (Kollmann, 2012), which will at least also apply to $L \geq 7$ because neutral torus densities are falling more rapidly with increasing L than the I/F of the E-ring (e.g., Hood, 1983; Krupp, Kollmann, et al., 2018). Energy loss effectively shifts a phase space density spectrum to lower energies. If the spectrum is continuously falling, every given energy will experience a loss of particles over time. This is described as (Kollmann et al., 2013; Schulz & Lanzerotti, 1974)

$$\frac{f}{\tau} = -\frac{v}{p^2}\frac{\partial}{\partial E}\left(p^2 f(E)\frac{\mathrm{d}E}{\mathrm{d}x}\right) \tag{7}$$

where v, p, and E are speed, momentum, and kinetic energy of the charged particle. $\mathrm{d}E/\mathrm{d}x$ is the energy loss of the particle per traversed distance x in material.

$\mathrm{d}E/\mathrm{d}x$ depends on the species and density of the material, in our case the Neutral Torus. We approximate it as consisting of H_2O and O and use tabulated values for $\mathrm{d}E/\mathrm{d}x$ applicable under standard conditions (Berger et al., 2005). These values are then linearly scaled to the Torus density at each respective distance. Our density model assumes a simple exponential decay with L-shell, starting from $L = 4$, where the Neutral Torus density peaks (see Figure S3 in Supporting Information S1). Density slopes and peak values are consistent with observations (Cassidy & Johnson, 2010; Melin et al., 2009) and generally fall within the range reported in more recent studies (e.g., Smith & Richardson, 2021).

In order to get a first estimate if Equation 7 provides an important contribution to Equation 1, we assume that $f(E)$ at all times close to the observed average f_0, which allows us to simply solve for τ in Equation 7. Results are shown in Figure 1b. The impact of τ under this approximation on $f(t)$ will be discussed in Section 4.

2.5. Local Diffusion

Whistler-mode chorus and hiss waves play an important role in shaping electron dynamics within Saturn's radiation belts. Chorus waves are observed across most local times, with their intensity peaking on the night side within the range of $4.5 < L < 7.5$ (Menietti et al., 2014). Chorus waves at Saturn are limited to the latitude range $0° < \lambda < 25°$. These waves are highly effective in accelerating electrons, particularly in low-density regions

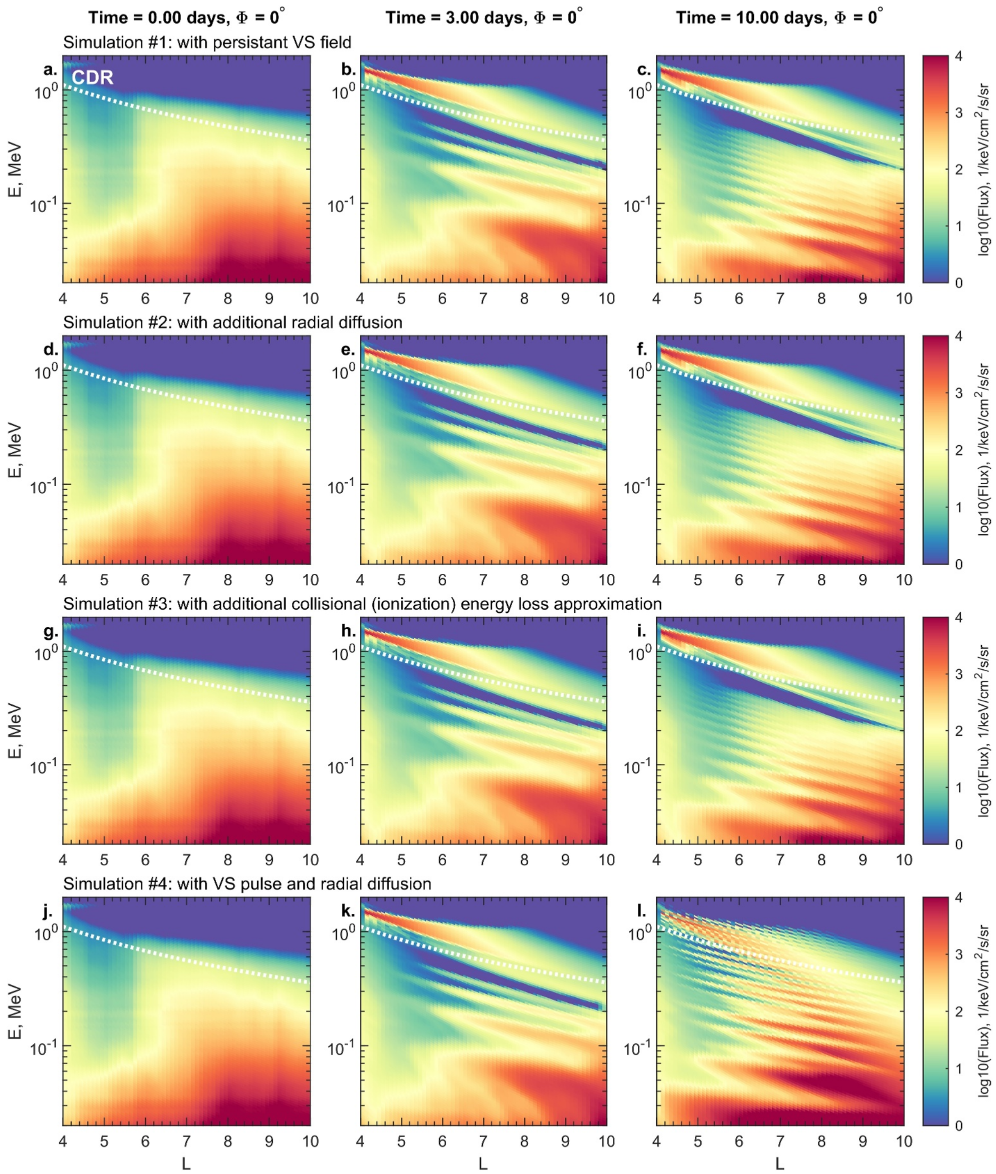

Figure 2. The electron flux from Versatile Electron Radiation Belt code simulation at equatorial pitch angle of ∼90° as a function of L-shell and energy at three time steps: 0 days (initial conditions), 3 and 10 days. Dashed white line shows the Corotation Drift Resonance energy. (a–c) Results of Simulation #1, which includes convection terms and persistent VS electric field. (d–f) Results of Simulation #2, based on Simulation #1, with additional radial diffusion term. (g–i) Results of Simulation #3, based on Simulation #2, with an additional approximation of collisional energy loss. (j–l) Results of Simulation #4, similar to Simulation #2 (with radial diffusion), but with VS electric field disabled after 3 days, imitating electric pulse and dynamical electric field configuration.

between $L \approx 2.5$ and 5.5 where the ratio of plasma frequency to gyro-frequency is less than 1 (Woodfield et al., 2019).

In contrast, hiss waves are ubiquitous, but structured primarily by L-shell, and observed at higher latitudes ($\lambda > 25°$) (Menietti et al., 2019). While typically associated with electron scattering at Earth, hiss waves at Saturn contribute to electron acceleration under low-density conditions (Woodfield et al., 2022). Additionally, wave-particle interactions involving Z-mode waves can also accelerate electrons, but the impact of these waves is primarily constrained within the orbit of Enceladus (Woodfield et al., 2018; Yu et al., 2019) and is not considered in this study. Electron cyclotron harmonic (ECH) waves have also been shown to significantly scatter low-energy electrons (∼10 eV to a few keV) and shape butterfly pitch-angle distributions at Saturn (Long et al., 2023). However, their effect lies outside the energy range considered in this study and is therefore not included.

In this study, we use bounce and drift-averaged diffusion coefficients corresponding to chorus and hiss waves (Woodfield et al., 2019, 2022). The chorus coefficients have been updated to use the same background plasma density model as those for the hiss waves, namely (Persoon et al., 2020), but all other parameters remain the same as in (Woodfield et al., 2019). Wave-particle interaction diffusion coefficients have been calculated using the Pitch Angle and Energy Diffusion of Ions and Electrons (PADIE) code (Glauert & Horne, 2005) and include many different wave and background plasma parameters: wave strength, wave frequency, wave normal angle, cold plasma density, background magnetic field strength. These coefficients are then converted to the V–K space using the technique described by Subbotin and Shprits (2012) and linearly interpolated to the simulation grid using normalized coordinates. The relatively limited observation data set at Saturn compared to the Earth is such that to obtain global coverage of the coefficients, parameters are derived from a mixture of empirical averaged data and models. This unfortunately loses any effects temporal variability may have on the diffusion coefficients, as explored recently at Earth by (e.g., Watt et al., 2021).

3. Simulations

We perform multiple 10-day simulations of Saturn's electron belt evolution, incorporating radial diffusion, convection, collisional energy loss, and local diffusion processes. The simulations time step is 15 min, however to ensure the stability of the convection calculation, the time step for convection is automatically adjusted according to the Courant-Friedrichs-Lewy Condition (see Aseev et al., 2016). These simulations allow us to evaluate the relative contributions of each mechanism to the overall electron dynamics. The electron flux is converted to phase space density and interpolated onto the simulation grid, providing initial and boundary conditions. Logarithmic extrapolation is applied to preserve the spectral slope, and the pitch-angle distribution is assumed to follow a sin function, which is the most commonly observed shape at $4 < L < 10$ (Clark et al., 2014; Yuan et al., 2021). The initial spectrum remains identical across all simulations and obtained from the observations without zebra stripe patterns (a mission average profile). This allows us to investigate mechanisms responsible for their formation and dynamics. We expect that a model that fully and accurately represents reality develops a zebra stripe pattern but over time averages out to the observed mission-average that we also use as initial condition.

3.1. Simulation Grid

The simulation grid consists of four key dimensions: the phase of magnetic local time (P), L-shell (L), and two adiabatic invariants, K and V. The magnetic local time phase spans from 0° to 360°, discretized into 25 points, including an overlapping point to ensure periodic boundary conditions. The L-shell ranges from 4 to 10, divided into 61 points with a resolution of 0.1. We use dipole approximation of the magnetic field in which L is equal to R in the equatorial plane.

The adiabatic invariants K and V are constructed at the upper L boundary using pitch-angle values ranging from 0.7° to 89.3° and energy values spanning 10 keV to 10 MeV. The K parameter includes 91 grid points linearly spaced along the pitch angle, while V is logarithmically spaced into 240 points along the energy axis. The high-resolution in energy grid is chosen to study the details of zebra stripe structure.

3.2. Simulation Scenarios

To isolate the effects of different physical processes, we structure our simulations into distinct scenarios. The first group of simulations (numbered #1 to #4) is conducted in three-dimensional (3D) space without considering the K (or pitch angle) dimension. In these cases, electron evolution is modeled at a fixed equatorial pitch angle of approximately of 90°. These simulations incorporate contributions from the VS and corotation electric fields, as well as magnetic fields, which drive the dominant transport processes that result in radial and azimuthal velocities.

The VS model is implemented in two configurations: persistent and pulsed. This setup allows us to investigate the role of electric field dynamics in electron acceleration, particularly in the ∼MeV energy range above CDR, and the formation of zebra stripe patterns. In the pulsed configuration, the electric fields E_{Φ}^{VS} and E_{R}^{VS} are deactivated after 3 days, imitating a transient variation. This approach enables an analysis of the subsequent evolution of the electron spectrum in the absence of the VS field, providing insight into how electric field variations affect

Table 1
Simulation Configurations and Parameters

Simulation #	Dimension	VS	Radial diffusion	Loss term	Local diffusion
1	3D	Persistent			
2	3D	Persistent	+		
3	3D	Persistent	+	Collisional energy loss	
4	3D	Pulse	+		
5	4D	Persistent	+	Loss cone	+
6	4D	Pulse	+	Loss cone	+

Note. The "Dimension" column specifies whether the setup is in 3D or 4D. The "VS" column indicates whether a persistent or 3-day pulsed Volland-Stern electric field was applied. The "Radial Diffusion" and "Local Diffusion" columns indicate the inclusion (+) of these processes. The "Loss Term" column distinguishes between collisional energy loss τ, as described in Equation 1, and losses due to the planetary loss cone boundary condition τ_{lc}, as described in Equation 2.

radiation belt dynamics. Additionally, in first group of simulations we examine the contributions of radial diffusion and collisional energy loss to electron dynamics.

The second group of simulations (#5 and #6) is performed in four-dimensional (4D) space, incorporating the K dimension along with local diffusion terms that account for interactions with chorus and hiss waves. As in the previous cases, these simulations are conducted in both persistent and pulsed VS electric field configurations. In these simulations, losses are driven by pitch-angle diffusion and the corresponding precipitation into the loss cone, as described in Equation 2. Table 1 summarizes the simulation setups, listing each simulation number.

4. Results

To analyze the simulation results, we construct the electron flux energy spectrum as a function of the L-shell. We focus on spectrum snapshots taken at the azimuthal location $\Phi = 0°$, corresponding to the magnetosphere's dayside (or noon in magnetic local time). Results at other magnetic local times show qualitivaly the same behavior and included in Supporting materials (see Figures S4–S9 in Supporting Information S1).

4.1. Effects of Radial Diffusion and Collisional Energy Loss on Zebra Stripes

Figure 2 presents spectrum snapshots from the first group of 3D simulations (#1 to #4), illustrating the initial conditions alongside the spectrum's evolution after 3 and 10 days. Figures 2a–2c shows the formation of zebra stripes in Simulation #1, which accounts for azimuthal and radial drift velocities under a persistent VS electric field and dipole magnetic field. These results closely replicate the test-particle simulations by Hao et al. (2020), but are derived using a convection code by solving Equation 1. The successful reproduction of the zebra-stripe signature validates our approach in capturing key electron dynamics observed in test-particle simulations.

The second row in Figures 2d–2f presents results from Simulation #2, which extends Simulation #1 by including radial diffusion. A comparison of the electron energy spectra after 10 days (e.g., Figure 2c vs. Figure 2f) reveals minimal variation. Figure 3a quantifies these differences on a logarithmic scale, showing an average deviation of only 0.03. These results indicate that radial diffusion is insufficient to disrupt zebra stripes formation on the timescales studied here. Radial diffusion may still play a critical role in setting up our assumed initial condition, which is a process that occurs on longer time scales that are beyond the scope of this study.

The persistent appearance of zebra stripes suggests that their formation is primarily controlled by convective processes, emphasizing the dominant role of large-scale electric fields over radial diffusion. We performed the simulation similar to simulation #1 but without VS field (no shown) which resulted in no significant change of initial flux and did not resulted in zebra stripes. Since, zebra stripes do not always appear in the observations, this suggest that other factors may affect their formation. One of these factors may be time-variability of VS field. We simulate such changes in simulations #4 and #6.

The next row in Figures 2g–2i presents results from Simulation #3, which extends Simulation #1 by incorporating collisional energy loss. This simulation excludes radial diffusion to isolate the specific impact of the additional loss term (see Section 2.4). As in the previous case, a comparison of the electron spectrum evolution after 10 days

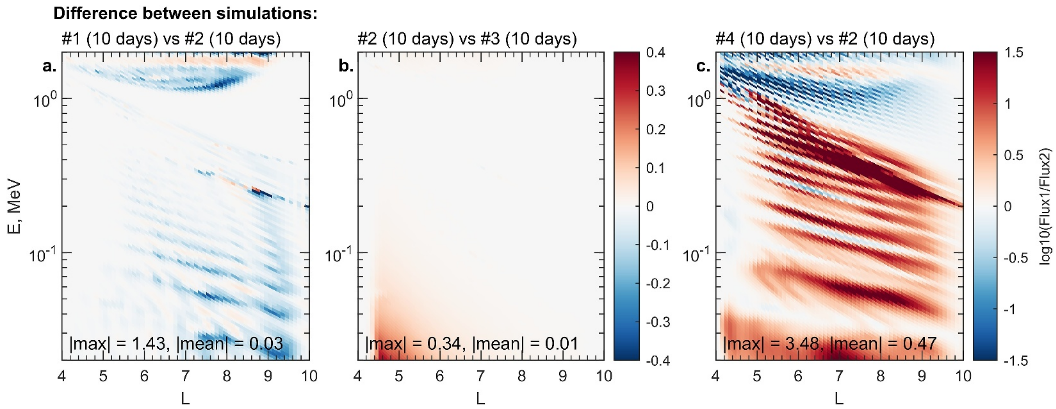

Figure 3. Logarithmic electron flux differences between simulations. The colorbar indicates the logarithmic difference of flux between chosen simulations and specified time. Maximum and mean absolute differences are annotated on each panel. (a) Difference between Simulation #1 and Simulation #2 after 10 days, indicating the influence of radial diffusion on zebra stripes. (b) Difference between Simulation #2 and Simulation #3 after 10 days, indicating a contribution of approximated collisional (ionization) energy loss. (c) Difference between Simulation #4 and Simulation #2 after 10 days, indicating the contribution of corotation electric field and radial diffusion in the absence of VS field.

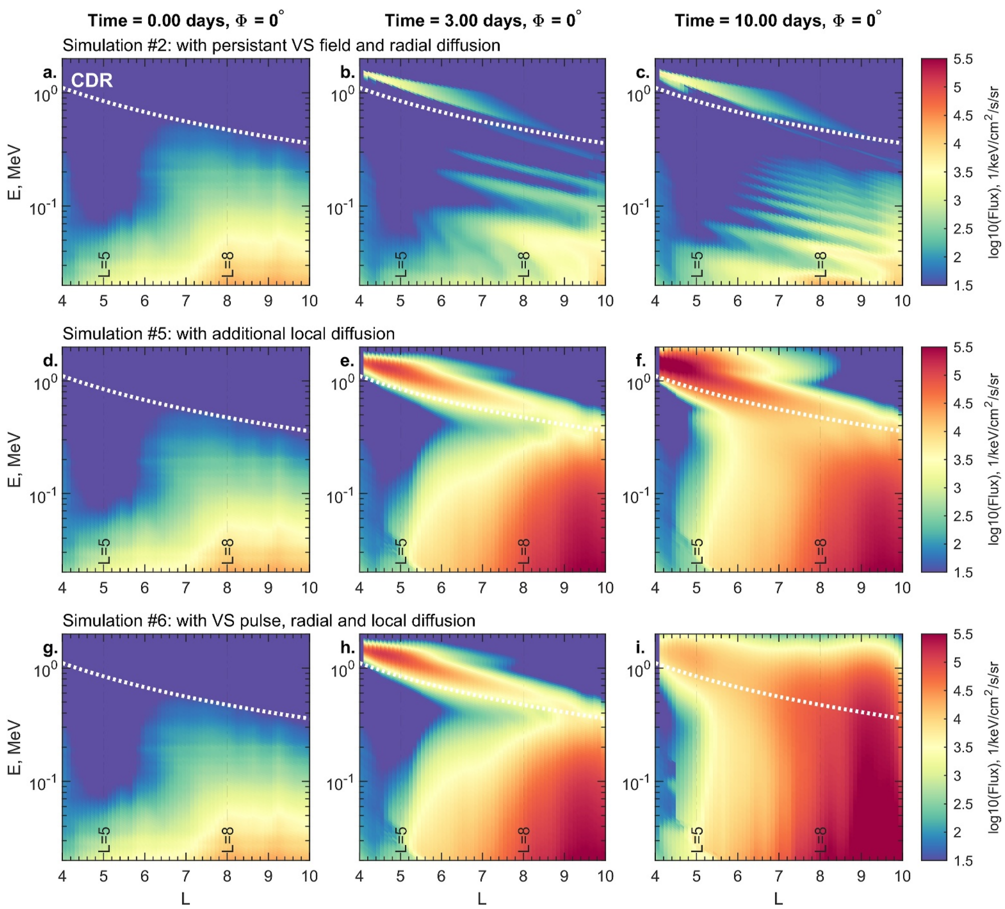

Figure 4. The electron flux from Versatile Electron Radiation Belt code simulation at equatorial pitch angle of $\sim 90°$ as a function of L-shell and energy for the time of 0 days (initial conditions), 3 and 10 days. Dashed white line shows the Corotation Drift Resonance energy. (a–c) Simulation #2, with enabled convection terms and persistent VS electric field and radial diffusion. (d–f) Simulation #5: based on Simulation #2, with additional local diffusion terms reflective wave-particle interaction due to hiss and chorus waves. (g–i) Simulation #6: based on Simulation #5, with VS electric field disabled after 3 days, imitating electric pulse and dynamical electric field configuration.

(e.g., Figure 2c vs. Figure 2i) reveals no significant changes. The logarithmic difference in Figure 3b shows that the additional loss term primarily affects the spectrum at $L < 7$ and energies below 100 keV, with an average difference of 0.01 across the entire spectrum. Thus, collisional energy loss under our approximation has a minimal impact on the electron population and does not influence zebra stripe formation. However, given that most model spectra significantly differ from the assumed average phase space density, our approximation may not be accurate. Calculating collisional energy loss self-consistently, in a time dependent manner instead of approximating it with its average value (through avoiding the approximation of using f_0 instead of $f(E)$ in the right hand side of Equation 7), may resolve the data-model discrepancies found in runs #5 and #6, discussed below.

The last row in Figures 2j–2l presents results from Simulation #4, which extends Simulation #1 by including radial diffusion and VS electric field in a pulsed configuration. As expected, Figure 2e (3 days of Simulation #2) and Figure 2k (3 days of Simulation #4) are identical. However, in Simulation #4, the VS electric field is deactivated after 3 days. Figure 2l shows that after 10 days, zebra stripe formation continues due to the asymmetry in the energy spectrum across magnetic local time that developed after 3 days of simulation. Moreover, the stripes tend to become denser and shift toward lower energies. Figure 3c presents the logarithmic difference between Simulation #4 and #2 after 10 days, showing an average difference of 0.47. Below the ∼MeV range, the difference indicates enhanced electron flux in Simulation #4, while a general depletion is seen at higher energies (above the CDR). Hence, the persistent corotation electric field continues to redistribute the energy spectrum and may eventually lead to the diminishing of zebra stripe structures initially formed by the pulsed VS electric field.

4.2. Impact of Local Diffusion on Spectrum Evolution

A feature that all model runs discussed above had in common is that drifts in the VS field let electrons accumulate just above CDR energies, forming an intensity peak at MeV energies, a behavior which is not observed. In the following, we are investigating if local diffusion may yield smoother spectra.

Figure 4 is similar to Figure 2 but presents spectrum snapshots from the second group of 4D simulations (#5 and #6), with Simulation #2 from the first group included for reference. In the 4D simulations, the spectra are shown at a equatorial pitch angle of $\sim 90°$ (88.6°), which is one grid point below the bounday. This figure highlights the impact of local diffusion, and due to the pronounced acceleration effects, it uses a different color scale with higher flux values. The second row in Figures 4d–4f illustrates the spectrum evolution of Simulation #5, which includes convection, radial diffusion, and local diffusion from hiss and chorus waves. Radial diffusion is here only added for completeness, but has no significant effect on the results. The last row in Figures 4g–4i presents results from Simulation #6, which is similar to Simulation #5 but performed with a pulsed VS field configuration.

Both simulations indicate that local diffusion is able to smooth the peak above CDR energies at large L-shells. On the other hand, under persistent VS field, local diffusion makes the peak at low L-shells more pronounced. We suggest that this behavior may resolve when treating collisional energy loss self-consistently. This effect can be most important at low L-shells where the Neutral Torus is most dense, but may also affect all other L-shells, due to the vast extent of the torus. Energy loss scales with $\partial f/\partial t$, which is high around the peak, particularly higher than in our assumption. The balance of local diffusion and energy loss ultimately may yield a spectrum close to observation.

Additionally, local diffusion suppresses zebra stripe formation. Therefore, when zebra stripes are observed, it implies that either the VS electric field is stronger than assumed—which is possible due to its known variability and incomplete constraints (e.g., Andriopoulou et al., 2014)—or that local diffusion is weaker than assumed, which may occur if these waves are not consistently present (e.g., Menietti et al., 2014). Wave power varies with universal time, local time and L-shell like the other parameters used to calculate the local diffusion coefficients. The averages and model values we use to calculate these coefficients are based on many years of data, which do not capture the temporal variability in diffusion rates experienced by electrons driven by the VS electric field. For example, at any given L-shell (when summed over all local times), hiss wave power can vary by several orders of magnitude (Menietti et al., 2019).

While the final spectra after 10 days differ slightly between simulation #5 (Figure 4f) and simulation #6 (Figure 4i), the flux remains significantly higher than in simulation #2 (Figure 4c) and are therefore higher than observed. While observations fluctuate about an order of magnitude away from the average in each direction (Kollmann et al., 2011), the discrepancies here are several orders of magnitude. This behavior may result from

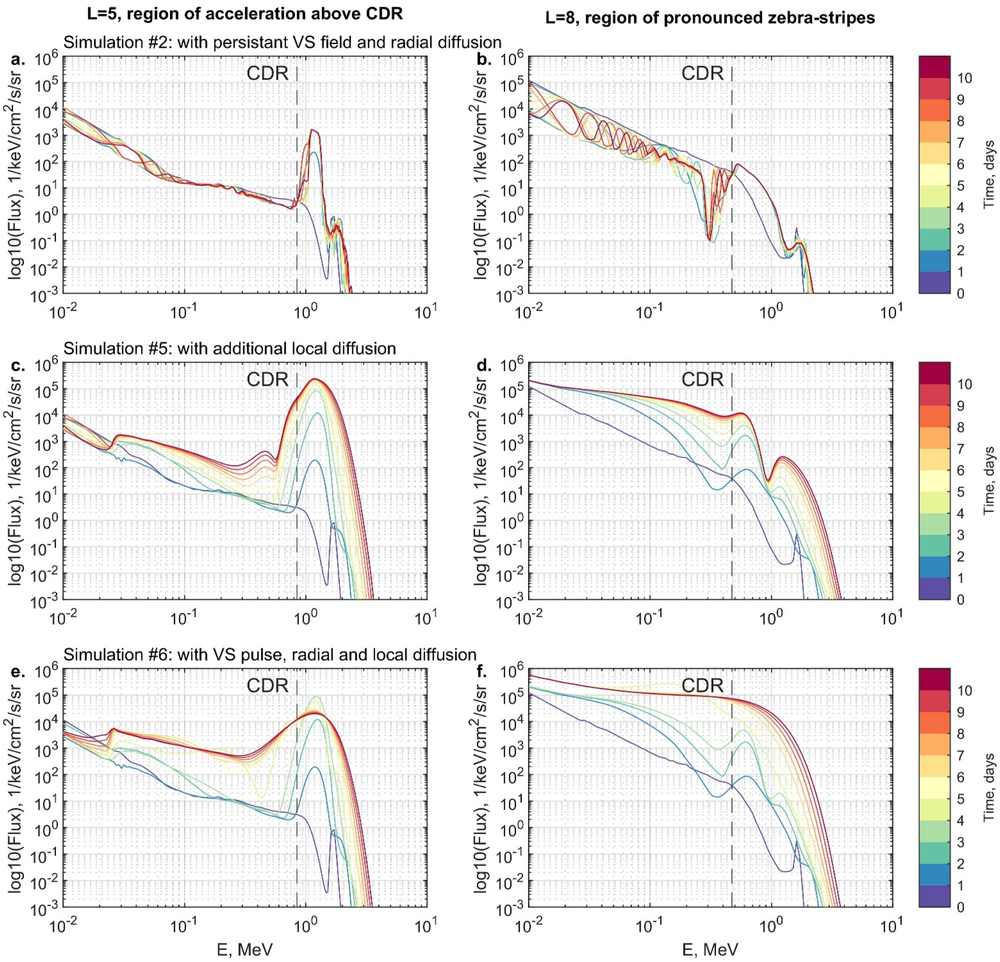

Figure 5. Evolution of the electron flux spectrum over time at $L = 5$ (left column, region of acceleration above the critical energy of radial diffusion, Corotation Drift Resonance (CDR)) and $L = 8$ (right column, region of pronounced zebra-stripes). The color gradient represents time from 0 to 10 days. Dashed line shows the CDR energy. (a), (b) Simulation #2, persistent VS field and radial diffusion. (c), (d) Simulation #5, additional local diffusion. (e), (f) Simulation #6, VS electric pulse imitating dynamical electric field configuration.

local diffusion not always being well represented by the assumed average value. Also collisional energy loss may be more important than in our approximation. In addition, accounting for wave-particle interaction due to electromagnetic ion cyclotron (EMIC) waves may improve the simulation results (Cao et al., 2023).

Figure 5 presents line plots of spectrum evolution at fixed $L = 5$ (left column) and $L = 8$ (right column), highlighting the pronounced spectral changes in simulations #2, #5 and #6. These locations are chosen to capture flux variations above CDR ($L = 5$) and the evolution of zebra stripes ($L = 8$).

A comparison between simulations at $L = 5$ (Figures 5a, 5c, and 5e) demonstrates that local diffusion significantly accelerates electrons above 1 MeV. However, the lower flux at the spectral peak in simulation #6 compared to simulation #5, along with the pronounced 1 MeV peak in simulation #2 (Figure 5a), suggests that the VS electric field is a key driver of electron acceleration above CDR. Although local acceleration is highly effective, in the absence of the VS field at the end of simulation #6, local diffusion smooths the spectrum, reducing electron flux levels. This indicates that while local diffusion contributes to electron energization, the VS field plays an important role in maintaining high flux levels, particularly in the ~MeV range.

Figure 5b shows the spectrum at $L = 8$, highlighting multiple local extrema that evolve over time—an indication of zebra stripe formation in simulation #2. Similarly, Figure 5d reveals the persistence of local extrema even after

10 days in simulation #5, where the persistent VS electric field continues to support zebra stripe formation, though with a reduced effect due to local diffusion. Finally, Figure 5f illustrates the spectrum from simulation #6, where the zebra stripe pattern is no longer visible after 10 days. Unlike Simulation #4, where the pattern remains preserved after the VS electric field is turned off, local diffusion in Simulation #6 dominates once the electric field is deactivated. As a result, the zebra stripes are gradually erased by energy diffusion, emphasizing the key role of local diffusion in suppressing the zebra stripe structures originally formed by the VS electric field.

Summarizing, the VS electric field is a key driver of electron acceleration, particularly above the CDR energies. A persistent VS field sustains electron acceleration, producing high-energy peaks. In contrast, when the VS field is turned off, the accelerated ∼MeV electron flux gradually dissipates due to local diffusion and spectral gradient changes. This demonstrates the combined influence of the VS field and local acceleration in shaping high-energy electron distributions. Additionally, local diffusion from chorus and hiss waves suppresses zebra stripe formation, indicating that it moderates the effects of the VS field and stabilizes electron spectra.

5. Conclusion

In this study, we examined how global and local physical processes influence electron acceleration and transport in Saturn's radiation belts. Our results demonstrate that the evolution of energetic electrons and the formation of zebra stripe patterns in spectrograms are predominantly driven by the Volland-Stern electric field.

Using the VERB convection-diffusion code, we successfully reproduced the zebra stripe signature, confirming the dominant role of the noon-to-midnight Volland-Stern electric field in shaping the electron energy distribution. In contrast, local diffusion processes due to interactions with chorus and hiss waves act to suppress zebra stripe formation, while the overall increasing electron flux across all energies. The zebra stripes are not always distinctly observed, and presented simulation results suggest, that while their formation depends on a large-scale electric field, their subsequent evolution and potential diminishing can continue under corotation-driven convection or local diffusion. Future research should focus on quantifying these temporal variations and their coupling with local diffusion processes to refine our understanding of electron dynamics in Saturn's magnetosphere. Additionally, comparison of the modeled spatial and energy structures with spacecraft observations should provide a quantitative assessment of the physical mechanisms at play. Further improvements may also come from including additional wave-particle interactions, such as those involving EMIC, Z-mode, or ECH waves.

Although radial diffusion likely plays a role to set up the initial distribution on which the Volland-Stern electric field is acting, it does not contribute to creating or disturbing the zebra stripe fine structure. Its potential temporal variability (e.g., Kollmann et al., 2017) may, however, affect electron distribution dynamics. Furthermore, our use of the Volland-Stern electric field represents a simplified and static approximation. Since Saturn's large-scale electric field can vary significantly in time and space, future studies should consider more realistic models, potentially based on MHD simulations (e.g., Sciola et al., 2021; Zhang et al., 2019), to better capture this variability and its impact on electron dynamics.

Our simulations also demonstrate the ability of both the Volland-Stern field as well as local diffusion to accelerate electrons beyond CDR energies. However, this behavior is not observed in measurements. Collisional energy loss does not contribute to spectral evolution within our model, however this is likely an artifact of our used approximation. In addition, we assume that pitch-angle scattering due to neutral collisions is negligible. Because electrons can scatter and may enter the loss cone, this assumption could contribute to the higher intensities observed at smaller L-shells and should be further investigated. In reality, energy loss may be able to counter acceleration processes to limit electron energies to their observed values.

Data Availability Statement

Cassini MIMI/LEMMS data can be obtained at https://pds-ppi.igpp.ucla.edu/collection/CO-S-MIMI-4-LEMMS-CALIB-V1.0, (Kusterer et al., 2024). The simulation results and data for presented figures and videos are available at UCLA Dataverse (Drozdov, 2025). The chorus and hiss diffusion coefficients are available via Zenodo (Woodfield, 2025).

Acknowledgments

This work was funded by NASA Grant 80NSSC21K0534. E. E. Woodfield was funded by STFC Grant ST/W00111X/1. This work used computational and storage services associated with the Hoffman2 Cluster which is operated by the UCLA Office of Advanced Research Computing's Research Technology Group. We also acknowledge Hayley Allison, Yuri Shprits, and the Cassini science team.

References

Andriopoulou, M., Roussos, E., Krupp, N., Paranicas, C., Thomsen, M., Krimigis, S., et al. (2012). A noon-to-midnight electric field and nightside dynamics in Saturn's inner magnetosphere, using microsignature observations. *Icarus*, *220*(2), 503–513. https://doi.org/10.1016/j.icarus.2012.05.010

Andriopoulou, M., Roussos, E., Krupp, N., Paranicas, C., Thomsen, M., Krimigis, S., et al. (2014). Spatial and temporal dependence of the convective electric field in Saturn's inner magnetosphere. *Icarus*, *229*, 57–70. https://doi.org/10.1016/j.icarus.2013.10.028

Aseev, N. A., Shprits, Y. Y., Drozdov, A. Y., & Kellerman, A. C. (2016). Numerical applications of the advective-diffusive codes for the inner magnetosphere. *Space Weather*, *14*(11), 993–1010. https://doi.org/10.1002/2016SW001484

Berger, M. J., Coursey, J. S., Zucker, M., & Chang, J. (2005). Stopping-power range tables electrons, protons, helium ions.

Cao, X., Lu, P., Ni, B., Summers, D., Shprits, Y. Y., Long, M., & Wang, X. (2023). Resonant scattering of radiation belt electrons at Saturn by ion cyclotron waves. *Geophysical Research Letters*, *50*(3), e2022GL102394. https://doi.org/10.1029/2022gl102394

Carbary, J. F., Mitchell, D. G., Krupp, N., & Krimigis, S. M. (2009). L shell distribution of energetic electrons at Saturn. *Journal of Geophysical Research*, *114*(A9), A09210. https://doi.org/10.1029/2009ja014341

Cassidy, T. A., & Johnson, R. E. (2010). Collisional spreading of Enceladus' neutral cloud. *Icarus*, *209*(2), 696–703. https://doi.org/10.1016/j.icarus.2010.04.010

Clark, G., Paranicas, C., Santos-Costa, D., Livi, S., Krupp, N., Mitchell, D. G., et al. (2014). Evolution of electron pitch angle distributions across Saturn's middle magnetospheric region from MIMI/LEMMS. *Planetary and Space Science*, *104*, 18–28. https://doi.org/10.1016/j.pss.2014.07.004

Drozdov, A. Y. (2025). Replication data for: Electron acceleration and zebra stripe formation in Saturn's radiation belts [Dataset]. *UCLA Dataverse*. https://doi.org/10.25346/S6/FHKLVZ

Drozdov, A. Y., Allison, H. J., Shprits, Y. Y., Elkington, S. R., & Aseev, N. A. (2021). A comparison of radial diffusion coefficients in 1-D and 3-D long-term radiation belt simulations. *Journal of Geophysical Research: Space Physics*, *126*(8), e2020JA028707. https://doi.org/10.1029/2020ja028707

Drozdov, A. Y., Shprits, Y. Y., Usanova, M. E., Aseev, N. A., Kellerman, A. C., & Zhu, H. (2017). EMIC wave parameterization in the long-term VERB code simulation. *Journal of Geophysical Research: Space Physics*, *122*(8), 8488–8501. https://doi.org/10.1002/2017JA024389

Drozdov, A. Y., Usanova, M. E., Hudson, M. K., Allison, H. J., & Shprits, Y. Y. (2020). The role of hiss, chorus, and EMIC waves in the modeling of the dynamics of the Multi-MeV radiation belt electrons. *Journal of Geophysical Research: Space Physics*, *125*(9), 2628. https://doi.org/10.1029/2020JA028282

Glauert, S. A., & Horne, R. B. (2005). Calculation of pitch angle and energy diffusion coefficients with the PADIE code. *Journal of Geophysical Research: Space Physics*, *110*(A4), A04206. https://doi.org/10.1029/2004JA010851

Hao, Y.-X., Sun, Y.-X., Roussos, E., Liu, Y., Kollmann, P., Yuan, C.-J., et al. (2020). The formation of Saturn's and Jupiter's electron radiation belts by magnetospheric electric fields. *The Astrophysical Journal Letters*, *905*(1), L10. https://doi.org/10.3847/2041-8213/abca3f

Hood, L. L. (1983). Radial diffusion in Saturn's radiation belts: A modeling analysis assuming satellite and ring E absorption. *Journal of Geophysical Research*, *88*(A2), 808–818. https://doi.org/10.1029/JA088iA02p00808

Horne, R. B., Thorne, R. M., Glauert, S. A., Douglas Menietti, J., Shprits, Y. Y., & Gurnett, D. A. (2008). Gyro-resonant electron acceleration at Jupiter. *Nature Physics*, *4*, 301–304. https://doi.org/10.1038/nphys897

Jones, G. H., Roussos, E., Krupp, N., Paranicas, C., Woch, J., Lagg, A., et al. (2006). Enceladus' varying imprint on the magnetosphere of Saturn. *Science*, *311*(5766), 1412–1415. https://doi.org/10.1126/science.1121011

Kempf, S., Beckmann, U., & Schmidt, J. (2010). How the Enceladus dust plume feeds Saturn's E ring. *Icarus*, *206*(2), 446–457. https://doi.org/10.1016/j.icarus.2009.09.016

Kollmann, P. (2012). *Sources, sinks, and transport of energetic particles within saturn's magnetosphere (Unpublished doctoral dissertation)*. Techn. Univ. Carolo-Wilhelmina.

Kollmann, P., Roussos, E., Kotova, A., Paranicas, C., & Krupp, N. (2017). The evolution of Saturn's radiation belts modulated by changes in radial diffusion. *Nature Astronomy*, *1*(12), 872–877. https://doi.org/10.1038/s41550-017-0287-x

Kollmann, P., Roussos, E., Paranicas, C., Krupp, N., & Haggerty, D. K. (2013). Processes forming and sustaining Saturn's proton radiation belts. *Icarus*, *222*(1), 323–341. https://doi.org/10.1016/j.icarus.2012.10.033

Kollmann, P., Roussos, E., Paranicas, C., Krupp, N., Jackman, C. M., Kirsch, E., & Glassmeier, K.-H. (2011). Energetic particle phase space densities at Saturn: Cassini observations and interpretations. *Journal of Geophysical Research: Space Physics*, *116*(A5), A05222. https://doi.org/10.1029/2010ja016221

Krimigis, S. M., Mitchell, D. G., Hamilton, D. C., Livi, S., Dandouras, J., Jaskulek, S., et al. (2004). Magnetosphere imaging instrument (MIMI) on the Cassini mission to Saturn/titan. *Space Science Reviews*, *114*(1–4), 233–329. https://doi.org/10.1007/s11214-004-1410-8

Krupp, N., Kollmann, P., Mitchell, D. G., Thomsen, M., Jia, X., Masters, A., & Zarka, P. (2018a). Global configuration and seasonal variations of Saturn's magnetosphere. In *Saturn in the 21st century* (pp. 126–165). Cambridge University Press. https://doi.org/10.1017/9781316227220.006

Krupp, N., Roussos, E., Kollmann, P., Mitchell, D. G., Paranicas, C. P., Krimigis, S. M., et al. (2018b). Energetic neutral and charged particle measurements in the inner Saturnian magnetosphere during the grand finale orbits of Cassini 2016/2017. *Geophysical Research Letters*, *45*(20), 10847–10854. https://doi.org/10.1029/2018gl078096

Kusterer, M. B., Manweiler, J., & Vandegriff, J. (2024). Cassini MIMI bundle [Dataset]. *NASA Planetary Data System*. https://doi.org/10.17189/6j8q-1397

Lejosne, S., & Kollmann, P. (2020). Radiation belt radial diffusion at earth and beyond. *Space Science Reviews*, *216*(1), 19. https://doi.org/10.1007/s11214-020-0642-6

Liu, Y., Zong, Q.-G., Zhou, X.-Z., Foster, J. C., & Rankin, R. (2016). Structure and evolution of electron "zebra stripes" in the inner radiation belt. *Journal of Geophysical Research: Space Physics*, *121*(5), 4145–4157. https://doi.org/10.1002/2015ja022077

Long, M., Cao, X., Ni, B., Lou, Y., Yao, Z., Roussos, E., et al. (2023). Formation of electron butterfly pitch angle distributions in Saturn's magnetosphere due to scattering by equatorial ECH waves. *Geophysical Research Letters*, *50*(19), e2023GL105318. https://doi.org/10.1029/2023gl105318

Melin, H., Shemansky, D. E., & Liu, X. (2009). The distribution of atomic hydrogen and oxygen in the magnetosphere of Saturn. *Planetary and Space Science*, *57*(14–15), 1743–1753. https://doi.org/10.1016/j.pss.2009.04.014

Menietti, J. D., Averkamp, T. F., Groene, J. B., Horne, R. B., Shprits, Y. Y., Woodfield, E. E., et al. (2014). Survey analysis of chorus intensity at Saturn. *Journal of Geophysical Research: Space Physics*, *119*(10), 8415–8425. https://doi.org/10.1002/2014ja020523

Menietti, J. D., Averkamp, T. F., & Kurth, W. S. (2019). Survey of Saturn whistler mode hiss intensity. *Journal of Geophysical Research: Space Physics*, *124*(6), 4266–4277. https://doi.org/10.1029/2019ja026656

Paranicas, C., Mitchell, D. G., Krimigis, S. M., Carbary, J. F., Brandt, P. C., Turner, F. S., et al. (2010). Asymmetries in Saturn's radiation belts. *Journal of Geophysical Research*, *115*(A7), A07216. https://doi.org/10.1029/2009ja014971

Paranicas, C., Thomsen, M. F., Kollmann, P., Azari, A. R., Bader, A., Badman, S. V., et al. (2020). Inflow speed analysis of interchange injections in Saturn's magnetosphere. *Journal of Geophysical Research: Space Physics*, *125*(9). https://doi.org/10.1029/2020ja028299

Persoon, A. M., Kurth, W. S., Gurnett, D. A., Faden, J. B., Groene, J. B., Morooka, M. W., et al. (2020). Distribution in Saturn's inner magnetosphere from 2.4 to 10 R_S: A diffusive equilibrium model. *Journal of Geophysical Research: Space Physics*, *125*(3), e2019JA027545. https://doi.org/10.1029/2019ja027545

Roussos, E., Jones, G. H., Krupp, N., Paranicas, C., Mitchell, D. G., Lagg, A., et al. (2007). Electron microdiffusion in the Saturnian radiation belts: Cassini MIMI/LEMMS observations of energetic electron absorption by the icy moons: Icy moon absorption signatures. *Journal of Geophysical Research*, *112*(A6), A06214. https://doi.org/10.1029/2006JA012027

Roussos, E., Kollmann, P., Krupp, N., Paranicas, C., Dialynas, K., Sergis, N., et al. (2018). Drift-resonant, relativistic electron acceleration at the outer planets: Insights from the response of Saturn's radiation belts to magnetospheric storms. *Icarus*, *305*, 160–173. https://doi.org/10.1016/j.icarus.2018.01.016

Roussos, E., Krupp, N., Paranicas, C., Carbary, J. F., Kollmann, P., Krimigis, S. M., & Mitchell, D. G. (2014). The variable extension of Saturn's electron radiation belts. *Planetary and Space Science*, *104*, 3–17. https://doi.org/10.1016/j.pss.2014.03.021

Saikin, A. A., Shprits, Y. Y., Drozdov, A. Y., Landis, D. A., Zhelavskaya, I. S., & Cervantes, S. (2021). Reconstruction of the radiation belts for solar cycles 17–24 (1933–2017). *Space Weather*, *19*(3), e2020SW002524. https://doi.org/10.1029/2020sw002524

Schulz, M., & Lanzerotti, L. J. (1974). *Particle diffusion in the radiation belts* (Vol. 7). Springer-Verlag Berlin Heidelberg.

Sciola, A., Toffoletto, F., Alexander, D., Sorathia, K., Merkin, V., & Farrish, A. (2021). Incorporating inner magnetosphere current-driven electron acceleration in numerical simulations of exoplanet radio emission. *The Astrophysical Journal*, *914*(1), 60. https://doi.org/10.3847/1538-4357/abefd9

Shprits, Y. Y., Daae, M., & Ni, B. (2012). Statistical analysis of phase space density buildups and dropouts. *Journal of Geophysical Research*, *117*(A1), A01219. https://doi.org/10.1029/2011JA016939

Shprits, Y. Y., Kellerman, A. C., Drozdov, A. Y., Spence, H. E., Reeves, G. D., & Baker, D. N. (2015). Combined convective and diffusive simulations: VERB-4D comparison with 17 March 2013 Van Allen probes observations. *Geophysical Research Letters*, *42*(22), 9600–9608. https://doi.org/10.1002/2015GL065230

Shprits, Y. Y., Subbotin, D., & Ni, B. (2009). Evolution of electron fluxes in the outer radiation belt computed with the VERB code. *Journal of Geophysical Research: Space Physics*, *114*(A11), A11209. https://doi.org/10.1029/2008JA013784

Shprits, Y. Y., Subbotin, D. A., Meredith, N. P., & Elkington, S. R. (2008). Review of modeling of losses and sources of relativistic electrons in the outer radiation belt II: Local acceleration and loss. *Journal of Atmospheric and Solar-Terrestrial Physics*, *70*(14), 1694–1713. https://doi.org/10.1016/j.jastp.2008.06.014

Smith, H. T., Johnson, R. E., Perry, M. E., Mitchell, D. G., McNutt, R. L., & Young, D. T. (2010). Enceladus plume variability and the neutral gas densities in Saturn's magnetosphere. *Journal of Geophysical Research*, *115*(A10), A10252. https://doi.org/10.1029/2009ja015184

Smith, H. T., & Richardson, J. D. (2021). The 3D structure of Saturn magnetospheric neutral tori produced by the Enceladus plumes. *Journal of Geophysical Research: Space Physics*, *126*(3), e2020JA028775. https://doi.org/10.1029/2020ja028775

Subbotin, D. A., & Shprits, Y. Y. (2009). Three-dimensional modeling of the radiation belts using the versatile electron radiation belt (VERB) code. *Space Weather*, *7*(10), S10001. https://doi.org/10.1029/2008SW000452

Subbotin, D. A., & Shprits, Y. Y. (2012). Three-dimensional radiation belt simulations in terms of adiabatic invariants using a single numerical grid. *Journal of Geophysical Research*, *117*(A5), A05205. https://doi.org/10.1029/2011JA017467

Sun, Y. X., Roussos, E., Krupp, N., Zong, Q. G., Kollmann, P., & Zhou, X. Z. (2019). Spectral signatures of adiabatic electron acceleration at Saturn through corotation drift cancelation. *Geophysical Research Letters*, *46*(17–18), 10240–10249. https://doi.org/10.1029/2019gl084113

Ukhorskiy, A. Y., Sitnov, M. I., Mitchell, D. G., Takahashi, K., Lanzerotti, L. J., & Mauk, B. H. (2014). Rotationally driven 'zebra stripes' in earth's inner radiation belt. *Nature*, *507*(7492), 338–340. https://doi.org/10.1038/nature13046

Watt, C. E. J., Allison, H. J., Thompson, R. L., Bentley, S. N., Meredith, N. P., Glauert, S. A., et al. (2021). The implications of temporal variability in wave-particle interactions in Earth's radiation belts. *Geophysical Research Letters*, *48*(1), e2020GL089962. https://doi.org/10.1029/2020gl089962

Woodfield, E. E. (2025). Saturn electron radiation belt diffusion coefficients for chorus and hiss waves [Dataset]. *Zenodo*. https://doi.org/10.5281/ZENODO.14893128

Woodfield, E. E., Glauert, S. A., Menietti, J. D., Averkamp, T. F., Horne, R. B., & Shprits, Y. Y. (2019). Rapid electron acceleration in low-density regions of Saturn's radiation belt by whistler mode chorus waves. *Geophysical Research Letters*, *46*(13), 7191–7198. https://doi.org/10.1029/2019GL083071

Woodfield, E. E., Glauert, S. A., Menietti, J. D., Horne, R. B., Kavanagh, A. J., & Shprits, Y. Y. (2022). Acceleration of electrons by whistler-mode hiss waves at Saturn. *Geophysical Research Letters*, *49*(3), e2021GL096213. https://doi.org/10.1029/2021GL096213

Woodfield, E. E., Horne, R. B., Glauert, S. A., Menietti, J. D., Shprits, Y. Y., & Kurth, W. S. (2018). Formation of electron radiation belts at Saturn by Z-mode wave acceleration. *Nature Communications*, *9*(1), 5062. https://doi.org/10.1038/s41467-018-07549-4

Yu, J., Li, L. Y., Cui, J., Cao, J. B., & Wang, J. (2019). Combined effects of equatorial chorus waves and high-latitude z-mode waves on Saturn's radiation belt electrons. *Geophysical Research Letters*, *46*(15), 8624–8632. https://doi.org/10.1029/2019gl084004

Yuan, C.-J., Roussos, E., Wei, Y., Krupp, N., Sun, Y. X., & Hao, Y. X. (2021). Cassini observation of relativistic electron butterfly distributions in Saturn's inner radiation belts: Evidence for acceleration by local processes. *Geophysical Research Letters*, *48*(14), e2021GL092690. https://doi.org/10.1029/2021gl092690

Zhang, B., Sorathia, K. A., Lyon, J. G., Merkin, V. G., Garretson, J. S., & Wiltberger, M. (2019). GAMERA: A three-dimensional finite-volume MHD solver for non-orthogonal curvilinear geometries. *The Astrophysical Journal - Supplement Series*, *244*(1), 20. https://doi.org/10.3847/1538-4365/ab3a4c

References From the Supporting Information

Roederer, J. G. (1970). *Dynamics of geomagnetically trapped radiation*. Springer Berlin Heidelberg. https://doi.org/10.1007/978-3-642-49300-3